



Classification of diffuse light emission profiles for distinguishing skin layer penetration of a needle-free jet injection

KIERAN A. BRENNAN,^{1,*}  BRYAN P. RUDDY,^{1,2} POUL M. F. NIELSEN,^{1,2} AND ANDREW J. TABERNER^{1,2}

¹Auckland Bioengineering Institute, The University of Auckland, 70 Symonds Street, Auckland, New Zealand

²Department of Engineering Science, The University of Auckland, 70 Symonds Street, Auckland, New Zealand

*kbre995@aucklanduni.ac.nz

Abstract: In this work, a system is developed for tracking the skin layer to which a needle-free jet injection of fluid has penetrated by incorporating a laser beam into the jet, and measuring the diffuse light emitted from skin tissue. Monitoring the injection in this way offers the ability to improve the reliability of drug delivery with this transdermal delivery method. A laser beam, axially aligned with a jet of fluid, created a distribution of diffuse light around the injection site that varied as the injection progressed. High-speed videography was used to capture the diffuse light emission from laser-coupled jet injections into samples of porcine skin, fat, and muscle. The injection produced a distribution of diffuse light around the injection site that varied as the injection descended. A classifier, trained to distinguish whether the light source was located in the fat or muscle from surface intensity profile measurements, correctly identified the injected layer in 97.2% of the cases when cross-examined against estimates using the light distribution emitted from the side of the sample.

© 2019 Optical Society of America under the terms of the [OSA Open Access Publishing Agreement](#)

1. Introduction

Jet injection is an alternative transdermal drug delivery technique to the traditional needle and syringe method, whereby a liquid drug is accelerated through a small orifice to form a jet that penetrates through skin. There are many advantages to this approach, including reduced patient fear and increased compliance. However, the technique remains hindered by poor injection depth control, which can lead to pain and local swelling [1]. Furthermore, failing to inject a drug into the intended tissue layer can have adverse consequences [2]. For example, insulin is a drug commonly administered via jet injection into the subcutaneous fat. Accidentally injecting insulin into the muscle can lead to an absorption rate increase of up to 50% [3], which could have an unfavorable impact on the blood glucose regulation of a diabetic patient.

Previously, some researchers have attempted to improve the depth control achieved during injection by developing a predictive model, which described injection depth as a function of the jet and tissue parameters [4]. However, the properties of skin vary significantly between anatomical locations and are not easily determined. The parameters required to achieve penetration to a given depth can therefore vary greatly between patients and between injection sites on a patient. We have taken an alternative approach towards resolving this issue, by monitoring the depth of an injection in real time using spatially-resolved diffuse imaging.

The objective of this imaging technique is to determine the tissue layer that the fluid jet is penetrating into, which can then be used to target the correct layer by adjusting the jet speed accordingly. Many commonly jet injected drugs require delivery into either the fat (e.g. insulin) or into the muscle (e.g. vaccines) [1,5,6]. Distinguishing the penetration of these two layers during a jet injection is the subject of this paper.

Diffuse optical imaging is a commonly used method for determining local skin optical properties for applications including the quantification of chromophores and tracking structures embedded within tissue [7–12]. Methods of estimating the depth of a light source in tissue have previously involved an inversion of the analytical diffusion model of light propagation [13–15]. We have previously shown it is possible to recover source depth using a Monte Carlo-based polynomial model [16]. Our polynomial model produced depth estimates within 2 mm of the true source, down to a depth of 15 mm in tissue-mimicking phantoms. For the application to jet injection, we have developed a system to incorporate a laser beam into the fluid jet as it is injecting, which produces a depth-dependent spatial distribution of light on the skin surface [17]. We have shown that an appropriate inverse model can successfully recover the effective source depth from the surface intensity profile for injections into porcine tissue samples. However, the method developed was applicable only to quasi-homogeneous samples of fat-only and skin and fat. The significant difference in optical properties between fat and muscle means the light propagation differs substantially as the light source enters the muscle layer.

A different approach is proposed in this work, where the optical property mismatch between fat and muscle tissue is exploited to determine a characteristic change in the light distribution that occurs as the source transitions from fat into muscle. Laser-coupled injections were performed into excised samples of skin, fat, and muscle, and a set of analogous experiments was performed with a depth-controlled light source plunged into tissue. The light emitted from the side of the sample was used to determine which tissue layer the source was in and a classifier was trained to perform the same identification using only the surface intensity profile.

2. Materials and methods

A jet injection system was created, in which a laser beam was axially aligned with the jet of fluid during the injection. A system replicating the simplified scenario of a point light source within a tissue sample was also developed using a fiber optic light source plunged into tissue. Experiments with both systems were performed on samples of skin, fat, and muscle, and videography was used to capture the diffuse light emitted from the side and top surface of the samples.

2.1. Jet injection system

The jet injection system, coupled a laser beam into the jet of fluid (Fig. 1). The system is detailed in Ref. [18] and summarised here briefly. A piston, connected to a voice-coil motor, generated pressure in the fluid ampoule, forming a jet through the orifice on the underside of the ampoule. A T-shaped channel in the ampoule provided access for a laser beam to be directed through an acrylic window on the upper side and aligned with the orifice. The nozzle included a needle extending 2 mm into the sample, to breach the dermis. The small needle was required to lower the jet speed requirement of penetration to below the inception point of cavitation, thereby maintaining optical transparency in the injected fluid.

2.2. Depth-controlled source system

This proposed method builds upon the assumption that the laser beam is guided by the fluid and impinges on the tissue at the bottom of the jet. To replicate this scenario, a laser was coupled into an optical fiber, which was guided through a hypodermic needle and plunged into tissue (Fig. 2). The needle carrying the optical fiber was connected to a position-controlled voice coil motor, mounted vertically, providing accurate control of the depth trajectory.

2.3. Experiments

Samples of porcine skin, fat, and muscle were excised from the abdominal region of an approximately 3-month old pig, shortly after being euthanized, in accordance with the University

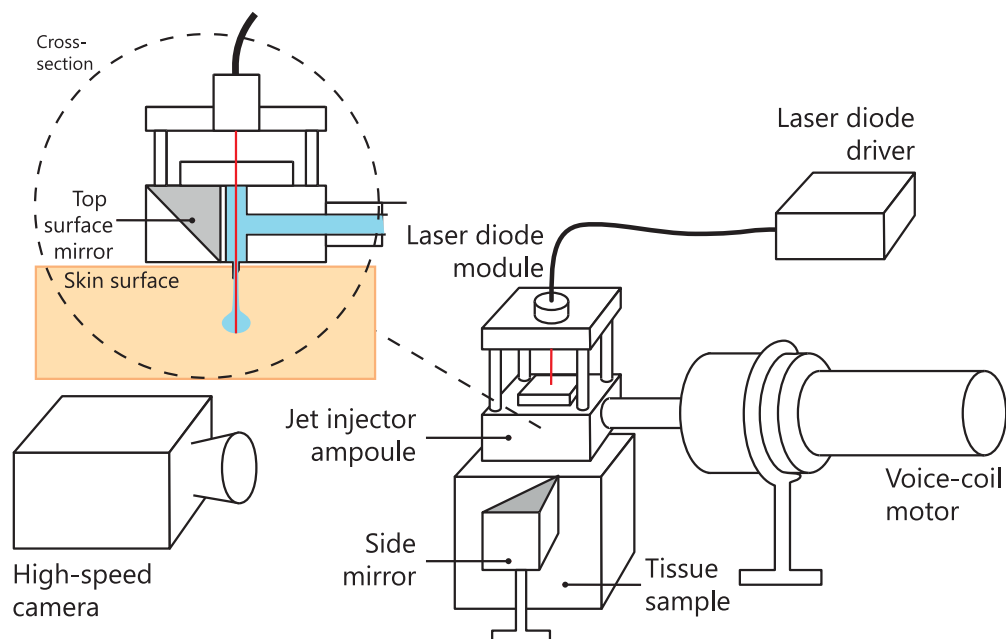


Fig. 1. Diagram of the injection system for coupling a laser into a jet of fluid as it is injected into tissue. A 2 mm needle extends from the orifice to pierce the toughest skin layer.

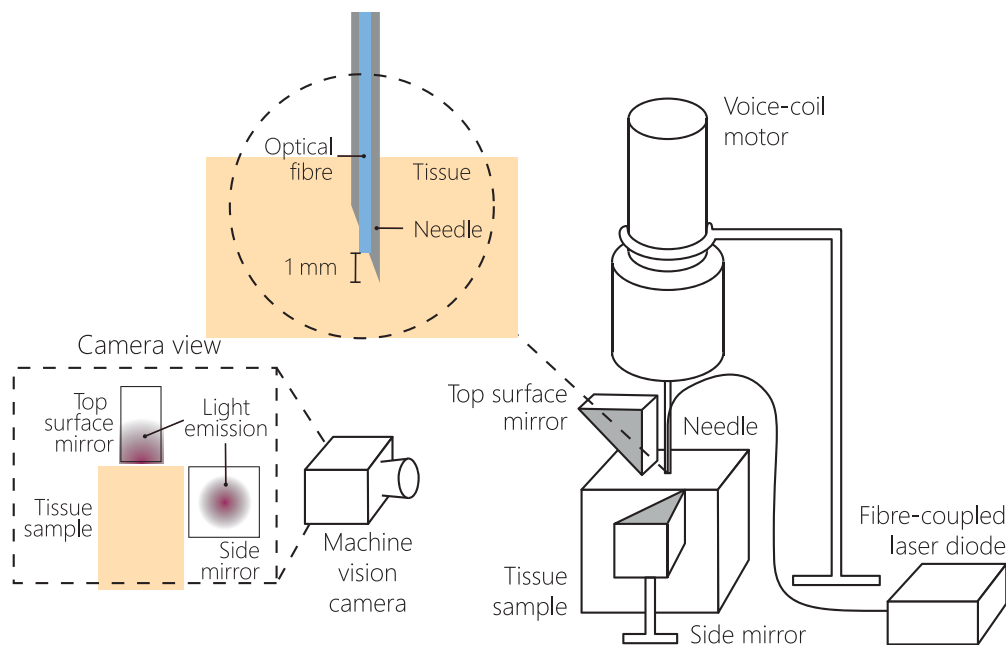


Fig. 2. Diagram of the system for controlling the descent of a fiber optical light source into tissue. A optical fibre is guided into tissue through a hypodermic needle.

of Auckland Code of Ethical Conduct for the Use of Animals for Teaching and Research. Ex vivo, abdominal porcine tissue has been shown to be a representative model of human skin [19], and epidermal and dermal thicknesses have been shown to be similar [20]. For these reasons, and its ready availability, ex vivo porcine skin the typical model used in jet injection studies [2,21]. All samples were stored in a -80° freezer and thawed to room temperature ($\sim 22^{\circ}$) prior to experimentation. Samples were excised to have a top surface area of $10\text{ mm} \times 30\text{ mm}$ and a depth of at least 20 mm , and were held in a transparent acrylic (poly(methyl methacrylate)) container with an acrylic cover plate. The depth of the fat-muscle boundary for each of the samples was measured from photographs captured prior to each injection. Figure 3a shows the ambiguity in identifying the boundary, which may introduce error. The depth of the ten samples used for each experiment is summarized in Fig. 3b.

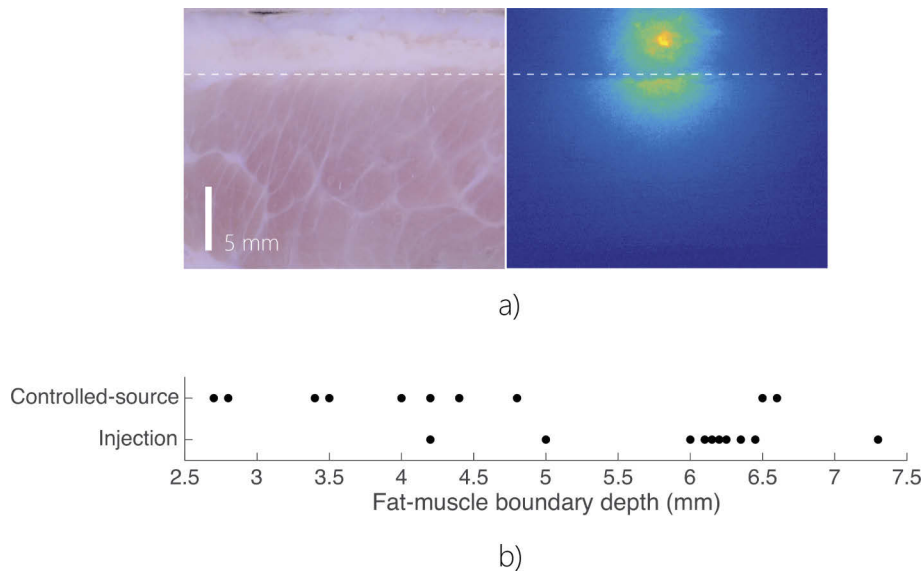


Fig. 3. a) Photograph of a tissue sample with the fat-muscle boundary indicated, and the corresponding view of the side distribution where the light source is approaching the boundary (false colour). b) Depth of the fat-muscle boundary (mm) below the skin surface for ten trials of each experiment type.

Experiments were performed using a high frame rate camera to capture the diffuse light emitted from the sample. The top and side surfaces of the samples were simultaneously viewed using two mirrors. The top surface was visible across a radial distance of 3 mm to 14 mm , subtending an angle of 23° , while a $25\text{ mm} \times 21\text{ mm}$ region was visible on the side surface.

2.3.1. Jet injection experiments

Injections of $200\text{ }\mu\text{L}$ of fluid were performed with a two-phase jet speed profile, involving a 165 ms^{-1} phase for 20 ms followed by a 95 ms^{-1} phase for 26 ms . The diffuse light emission was recorded at 5000 frames per second with a high-speed video camera (Phantom Miro M310), thereby capturing 230 frames during the injection.

After each injection, an X-ray image of the sample was acquired using a micro-CT imaging system (SkyScan 1172, Bruker). Two-dimensional images of each sample, imaging down the short axis of the sample, were captured five minutes after the injection.

2.3.2. Depth-controlled source experiments

The controlled-source experiments were performed with the needle light source beginning 2 mm below the skin surface, and plunged to a depth of 17 mm over 23 s. A machine vision camera (Model FL3-U3-13Y3M-C, PointGrey Research) captured the diffuse light emission at a rate of 25 frames per second, thereby capturing 575 frames during the descent, with the source moving 0.026 mm between frames.

2.4. Image processing

The sector containing the view of the top surface of the tissue was selected and the light distribution was averaged circumferentially to extract the surface profile. Inspection of the side view of the sample revealed that two modes in the light distribution arose as the light source approached the muscle layer (Fig. 4). This behavior was caused by the difference in optical properties between the fat and muscle. A method was developed to monitor the transition of the source between the fat and muscle, by comparing the relative light intensity emitted from the two layers. The depth of the fat-muscle boundary, d_m , was measured from photographs of each sample and the side light distribution was partitioned into two sections: from the top of the sample to the fat-muscle boundary; and from the boundary to twice the depth of the muscle. The image of the side light distribution, $I(x, z)$, was integrated in these two sections using the trapezoidal rule, to determine the total emission from the fat, I_f , and muscle, I_m :

$$I_f \approx \int \int_{x,z \leq d_m} I(x, z) \, dx \, dz$$

$$I_m \approx \int \int_{x, d_m < z \leq 2d_m} I(x, z) \, dx \, dz.$$

The ratio of the emission from the two layers was then calculated:

$$I_{mf} = \frac{I_m}{I_f}, \quad (1)$$

which, if less than 1, indicated that the total light emission from the fat exceeded that of muscle, while the opposite was true when the value exceeded 1. The maximum depth was selected as $2d_m$ to remove the influence that the relative layer thicknesses had on the integrated light emission.

2.5. Surface intensity profile analysis

A classifier was generated to determine whether an injection was penetrating into the fat or muscle using surface intensity profile measurements alone. The inputs to the model, the predictor variables, were surface intensity profile measurements from radial positions of 3 mm, 5 mm, 7 mm, and 9 mm. These locations were selected as a previous depth estimation technique demonstrated success using measurements from these positions [16]. The surface intensity profile measurements, y_i , at the i^{th} radial position, were normalized to cancel the effect of optical variation from sample to sample according to:

$$\bar{y}_i = \frac{y_i}{y_{1y_{i,d_0}}}, \quad (2)$$

where y_{d_0} refers to the surface intensity profile measured with the light source incident at the initial depth of the light source, 2 mm below the tissue surface.

The k -nearest neighbor algorithm was used to classify layer penetration based on the surface intensity profile measurements. This algorithm involves defining a dataset of labeled feature vectors $(P_j, Q_j), \dots, (P_N, Q_N)$, where, in the present case, the feature vectors, P_j , are the

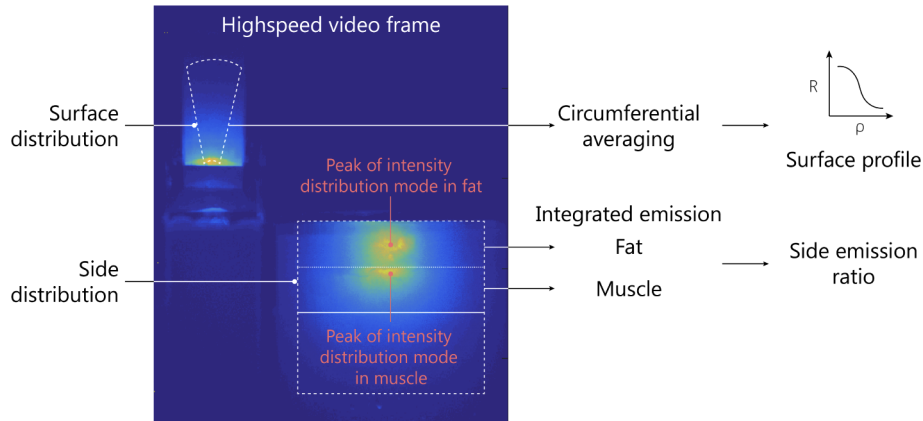


Fig. 4. Diagram showing the image processing of the high-speed video frames. The surface intensity profile is measured by averaging the view of surface distribution circumferentially. The side view of the sample exhibits two modes in the light distribution. The location of the light source is tracked using the ratio of the integrated emission between the fat and muscle.

normalized surface intensity profile measurements labeled with a binary variable, Q_j , designating whether the data were obtained with the source in the fat or in the muscle. When presented with a test vector, p , a prediction is generated by first evaluating the distance between p and each feature vector using a suitable metric:

$$w_j = \|P_j - p\|$$

The prediction is deemed as the most frequently occurring label of the k feature vectors with lowest distances, weighted by w_j . In our case, the Euclidean distance was used as the comparison metric, and k was set to 6. The classifier was generated using the *fitcknn* routine in MATLAB's Statistics and Machine Learning Toolbox (2016a, MathWorks).

3. Results

3.1. Controlled-source classification

3.1.1. Side distribution classification

The side emission ratio, I_{mf} , was plotted against source depth to determine whether consistent behavior occurred during penetration into the muscle, which could be used to distinguish which layer the source was in. To enable this analysis, the source depth was non-dimensionalized by the distance to the fat-muscle boundary, d_m , meaning that a value of 1 on the x -axis corresponds to the transition point between fat and muscle. The value of the side emission at this point is fairly consistent across trials, ranging from between 1.2 to 1.6 (Fig. 5).

A threshold was applied to the side emission ratio to classify the source as originating from either the fat or the muscle. The predictions were compared to the true site of the source to evaluate the specificity of the side emission ratio. The data in each trial were restricted to source depths between zero and $2d_m$. A threshold of 1.5 produced the greatest success, with only 4% of the data misclassified (Fig. 6). In the subsequent analysis of the jet injection experiments, the side emission ratio was used to identify the site of the effective source, as knowledge of the actual penetration depth was unavailable during the injection.

3.1.2. Surface intensity profile classification

Plotting the normalized surface profiles illustrates the distinction between those produced with the source in the fat versus profiles from when the source was in the muscle (Fig. 7). As the

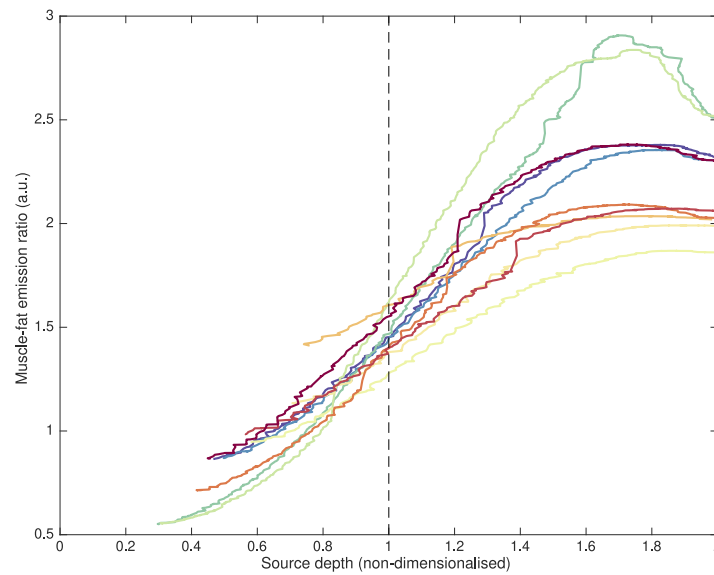


Fig. 5. Ratio of light emitted from fat and muscle for controlled-source experiments.

source descends, the surface intensity profile broadens, with the outermost value increasing the most relative to its initial value. The overlap between the two groups occurs in the transition zone between fat and muscle.

Leave-one-out cross validation (LOOCV) was used to assess the performance of the classifier across the ten controlled-source experiments. The data from each trial were successively tested using the remaining nine trials as the labeled feature vector set. The classification errors are much higher than for classification using the side emission metric, with incorrect classification in 16% of the test cases (Fig. 8). However, the errors are primarily clustered around the transition point between layers, which is expected due to the overlap of the surface intensity profiles in this region. Samples with a greater than average muscle depth (Trials 3 and 4) exhibit more frequent misrepresentations in the fat, while the reverse is true for samples with shallower muscle layers (Trials 6 and 7).

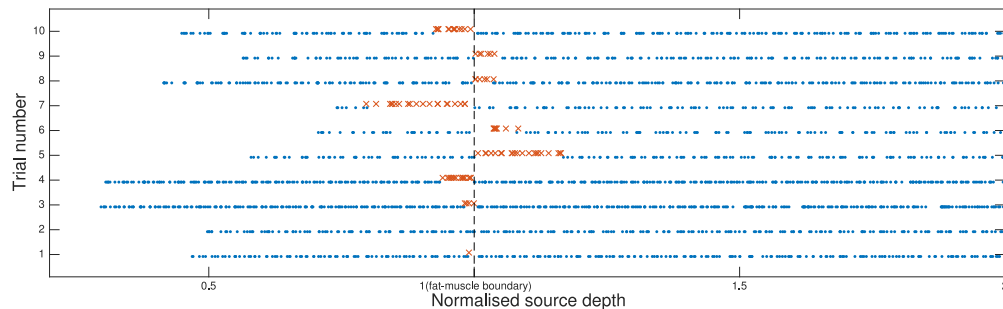


Fig. 6. Classification of the source layer by applying a threshold to the side light emission ratio. Successful classification is shown as blue dots, while orange cross represent incorrectly classified points. The dashed lines represents the muscle layer boundary.

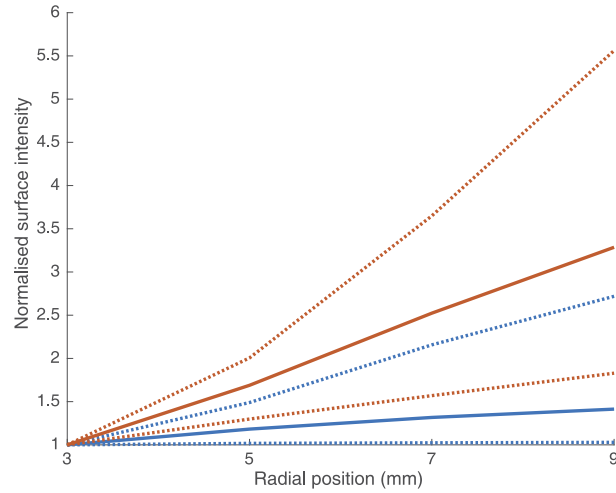


Fig. 7. Representative normalized surface intensity profiles from controlled-source experiments, labeled according to whether the source was in the fat (blue) or muscle (red). The median profiles are represented as solid lines and the dotted lines represent the 95-percentile profiles.

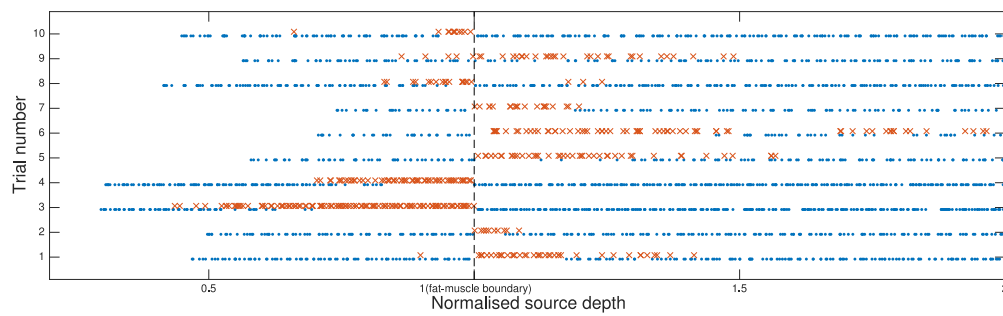


Fig. 8. LOOCV of layer classification from the surface intensity profile of controlled-source experiments, using k -nearest neighbor classification. Successful classification is displayed as blue dots while orange crosses represent incorrectly classified points. The dashed line represents the depth of the muscle boundary.

3.2. Jet injection classification

During a jet injection there was no means of verifying which layer the jet was penetrating into at a given point in time. Instead, only the final depth of delivery of the injections, determined from post-injection X-ray imaging, was used to confirm whether the light emission varied between the fat and muscle depending on the extent of the injection. For each point in time, the side emission ratio was then used to identify which layer the injection was penetrating into and a classifier was generated using the labeled surface intensity profiles.

3.2.1. Injection delivery depth

The post-injection X-ray images highlight the variability of injection penetration that can arise from a constant set of jet parameters (Fig. 9). Four of the injections penetrated through to the muscle layer (Trials 3, 4, 9, and 10) while the remaining six injections dispersed in the fat. Fluid delivery to the fat layer appears to produce a fairly consistent ellipsoidal bolus of fluid. Penetration into the muscle, on the other hand, appears striated, possibly due to the region between tissue fibers offering pathways of low resistance.

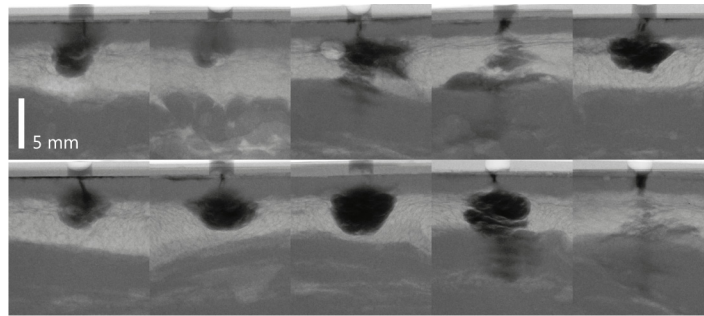


Fig. 9. Post-injection X-ray images of skin, fat, and muscle samples. Trials 1 through 10 are arranged left to right, top to bottom.

3.2.2. Side distribution classification

Equation 1 was used to calculate the ratio between light emitted from fat and muscle for each point in time. Charting the trajectory of this metric for each injection reveals a distinct difference in behavior between the intramuscular injections and the injections that remained in the fat (Fig. 10). Twenty milliseconds after the onset of the injection, the light emission in the muscle begins to increase markedly for the intramuscular injections. Thus, it appears that the effective light source transitions into the muscle layer, along with the penetration of the fluid, and that the side emission ratio is a useful metric for tracking this transition. To differentiate the frames when the effective source was in the fat from those in which the source was in the muscle, a value of 1.8 was selected as a threshold on the side emission ratio.

3.2.3. Surface intensity profile classification

The k -nearest neighbor algorithm was again used to classify layer penetration from the surface intensity profile. Inspection of the high-speed videos revealed that fluid pooled on the surface around the injection for three trials (1, 2, and 7). Data from these trials were excluded from the analysis as the surface intensity profiles were distorted from interference of the fluid. The remaining seven trials consisted of four intramuscular injections and three injections that remained in the fat.

The performance of the k -nearest neighbor classifier was assessed using LOOCV, giving 1610 tests of the algorithm using a set of 1380 feature vectors in each test case. The classification

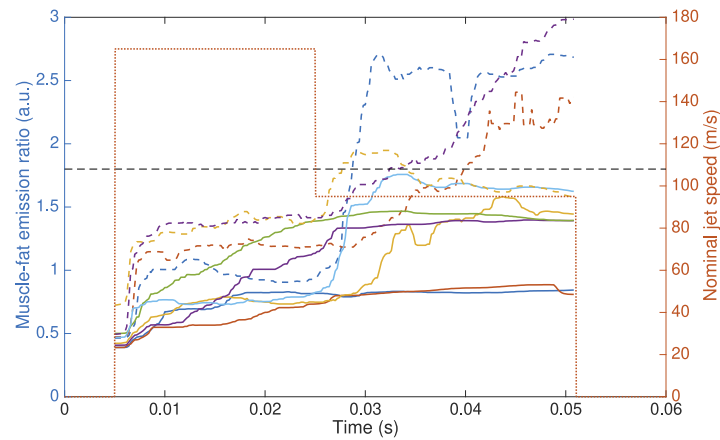


Fig. 10. Muscle-fat light emission ratio, calculated over the time course of ten injections. The injections that were delivered into the muscle are represented as dashed lines. The threshold for distinguishing layer penetration from the side emission ratio is represented as the dashed horizontal line. The dotted trace indicates the nominal jet speed profile for the injections.

success was indicated over the trace of side emission ratio (Fig. 11), showing that all injections into the fat were identified perfectly and only 3% of the data were incorrectly classified. The intramuscular injections were mostly classified correctly, with the misclassifications occurring close to the threshold. The classifier generated particularly poor predictions for Trial 9, depicted as yellow circles, misrepresenting almost every point where the effective source was in the muscle.

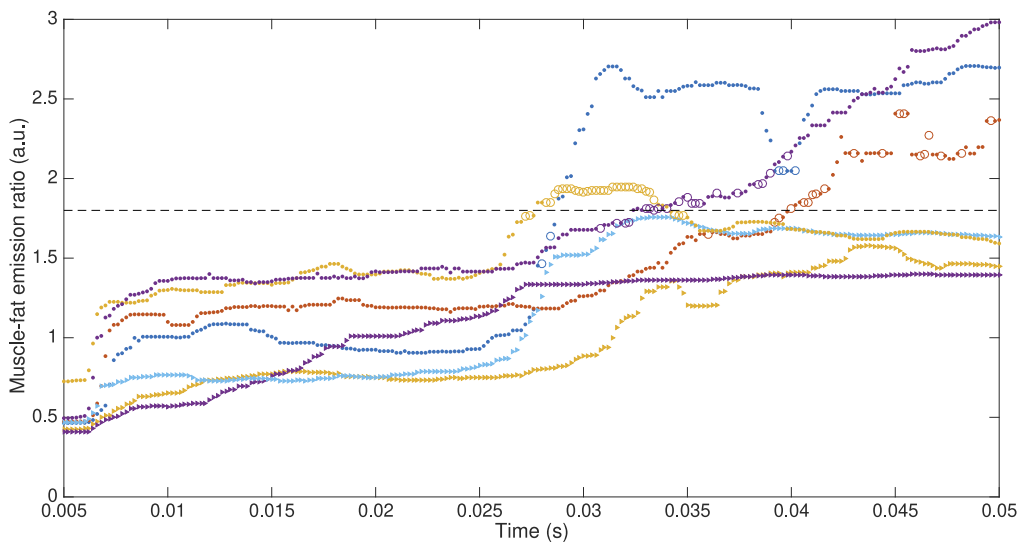


Fig. 11. LOOCV of distinguishing layer penetration from the surface intensity profile of jet injections, using k -nearest neighbor classification. Triangles represent the injections that remained in the fat and circles represent intramuscular injections. Successful classification is depicted with unfilled markers, while the unfilled markers represent incorrectly classified points. The dashed line represents the threshold on the side emission ratio used to label the data in the feature set.

However, the side metric only slightly exceeds the threshold, and from the post-injection X-ray (Fig. 9) it appears that the vast majority of the fluid was delivered into the fat.

4. Conclusions

A method of analysis was developed to distinguish the layer of light origination from the side light distribution. The ratio between light emitted from the fat and muscle was calculated and found to cross a consistent value as the source transitioned between the layers in the controlled-source experiments. Applying a threshold at this point made it possible to discern which layer the source was in from the side distribution alone. A k -nearest neighbor algorithm was used to classify the penetration of fat from muscle using surface intensity profile measurements from four radial locations. Leave-one-out analysis on the controlled-source experiments was successful at identifying the layer the light source was in in 83% of the cases.

The side emission ratio was confirmed as a suitable metric for distinguishing layer penetration in the jet injection experiments. Post-injection X-ray imaging identified four of the ten injections as penetrating to the muscle layer and those reached appreciably higher side emission ratio values than the injections that remained in the fat. A threshold was again applied to categorize the effective source as either in the fat or muscle, and leave-one-out validation was used to assess the performance of the k -nearest neighbor classifier. All injections that remained in fat were classified correctly as well as the majority of the data from the injections that reached the muscle. Misclassifications occurred only in the region near the threshold.

A classifier, trained on the surface light distribution, offers a viable method for distinguishing intramuscular injections from injections which remain in the fat layer. Furthermore, the method was successful for injections into samples with a range of muscle depths between 4.2 mm to 7.3 mm. Classification was, however, compromised for samples at the limits of muscle depth; the poorest prediction performance of the controlled-source trials was on the samples with the lowest muscle depths (2.6 mm, 2.7 mm) and greatest muscle depths (6.5 mm and 6.6 mm). Ideally, the feature dataset would be generated from samples with muscle depths which span a range that exceeds what would be expected in practice, to ensure that estimates at the extremes are not weakened. Further work with a larger feature dataset would be required to determine whether the classifier can generate reliable predictions over a wide range of layer thicknesses. Additional work would also be required to extend and validate this method over a wide range of skin optical and mechanical properties.

A real-time implementation of the classification routine could be used to inform the motor controller driving the injection. The layer prediction could be used to either increase or decrease the injection jet speed depending on whether the drug is required to be delivered to the fat or muscle. Incorrect estimates begin to occur around the transition point between layers, which could be used as an indicator that the injection is near the fat-muscle boundary. If the objective is to inject into fat, then any prediction that indicates penetration into the muscle would be cause to reduce the jet speed. Conversely, when performing intramuscular injections, the jet could be accelerated until there is no indication that the effective source remains in the fat.

Aside from the application to real-time control, the method presented here could provide a useful measure of injection success, helping inform the decision on how a clinician should proceed. For example, knowing that an intended intramuscular injection has remained in the fat may be crucial information for prompting a user to repeat administration of the drug. Furthermore, knowledge of the penetration depth over the time course of an injection could be used to provide an estimate of the proportion of fluid delivered into each layer.

Funding

MedTech Centre of Research Excellence (3505716); The University of Auckland Doctoral Scholarship.

Disclosures

The authors declare that there are no conflicts of interest related to this article.

References

1. S. Mitragotri, "Current status and future prospects of needle-free liquid jet injectors," *Nat. Rev. Drug Discovery* **5**(7), 543–548 (2006).
2. J. Schramm-Baxter and S. Mitragotri, "Needle-free jet injections: Dependence of jet penetration and dispersion in the skin on jet power," *J. Controlled Release* **97**(3), 527–535 (2004).
3. J. C. Thow, A. B. Johnson, G. Fulcher, and P. D. Home, "Different absorption of isophane (NPH) insulin from subcutaneous and intramuscular sites suggests a need to reassess recommended insulin injection technique," *Diabetic Med.* **7**(7), 600–602 (1990).
4. J. Schramm-Baxter, J. Katrencik, and S. Mitragotri, "Jet injection into polyacrylamide gels: Investigation of jet injection mechanics," *J. Biomech.* **37**(8), 1181–1188 (2004).
5. J. Baxter and S. Mitragotri, "Needle-free liquid jet injections: mechanisms and applications," *Expert Rev. Med. Devices* **3**(5), 565–574 (2006).
6. E. L. Giudice and J. D. Campbell, "Needle-free vaccine delivery," *Adv. Drug Delivery Rev.* **58**(1), 68–89 (2006).
7. T. Farrell, M. S. Patterson, and B. C. Wilson, "A diffusion theory model of spatially resolved, steady-state diffuse reflectance for the noninvasive determination of tissue optical properties in vivo," *Med. Phys.* **19**(4), 879–888 (1992).
8. J. S. Dam, P. E. Andersen, T. Dalgaard, and P. E. Fabricius, "Determination of tissue optical properties from diffuse reflectance profiles by multivariate calibration," *Appl. Opt.* **37**(4), 772–778 (1998).
9. A. Kienle, L. Lilge, M. S. Patterson, R. Hibst, R. Steiner, and B. C. Wilson, "Spatially resolved absolute diffuse reflectance measurements for noninvasive determination of the optical scattering and absorption coefficients of biological tissue," *Appl. Opt.* **35**(13), 2304–2314 (1996).
10. B. W. Rice, M. D. Cable, and M. B. Nelson, "In vivo imaging of light-emitting probes," *J. Biomed. Opt.* **6**(4), 432 (2001).
11. M. Sharma, R. Hennessy, M. K. Markey, and J. W. Tunnell, "Verification of a two-layer inverse Monte Carlo absorption model using multiple source-detector separation diffuse reflectance spectroscopy," *Biomed. Opt. Express* **5**(1), 40–53 (2014).
12. T.-Y. Tseng, C.-Y. Chen, Y.-S. Li, and K.-B. Sung, "Quantification of the optical properties of two-layered turbid media by simultaneously analyzing the spectral and spatial information of steady-state diffuse reflectance spectroscopy," *Biomed. Opt. Express* **2**(4), 901–914 (2011).
13. O. Coquoz, T. L. Troy, D. Jekic-McMullen, and B. W. Rice, Determination of depth of in vivo bioluminescent signals using spectral imaging techniques, in *Genetically Engineered and Optical Probes for Biomedical Applications* (International Society for Optics and Photonics, 2003), pp. 37–45.
14. D. C. Comsa, T. J. Farrell, and M. S. Patterson, "Bioluminescence imaging of point sources implanted in small animals post mortem: Evaluation of a method for estimating source strength and depth," *Phys. Med. Biol.* **52**(17), 5415–5428 (2007).
15. A. Kim, M. Roy, F. N. Dadani, and B. C. Wilson, "Topographic mapping of subsurface fluorescent structures in tissue using multiwavelength excitation," *J. Biomed. Opt.* **15**(6), 066026 (2010).
16. K. A. Brennan, D. A. N. Kulasingham, P. M. F. Nielsen, A. J. Taberner, and B. P. Ruddy, "High-speed light source depth estimation using spatially-resolved diffuse imaging," *J. Opt.* **21**(1), 015604 (2019).
17. K. Brennan, P. M. F. Nielsen, B. P. Ruddy, and A. J. Taberner, High speed, spatially-resolved diffuse imaging for jet injection depth estimation, in *Dynamics and Fluctuations in Biomedical Photonics XV*, vol. 10493 V. V. Tuchin, K. V. Larin, M. J. Leahy, and R. K. Wang, eds. (SPIE, 2018), p. 66.
18. K. A. Brennan, B. P. Ruddy, P. M. F. Nielsen, and A. J. Taberner, "High-speed depth estimation of needle-free jet injection using spatially-resolved diffuse imaging," *Submitt. to J. Biophotonics* (2019).
19. J. Baxter and S. Mitragotri, "Jet-induced skin puncture and its impact on needle-free jet injections: Experimental studies and a predictive model," *J. Controlled Release* **106**(3), 361–373 (2005).
20. T. P. Sullivan, W. H. Eaglstein, S. C. Davis, and P. Mertz, "The pig as a model for human wound healing," *Wound Repair Regen.* **9**(2), 66–76 (2001).
21. J. Schramm and S. Mitragotri, "Transdermal drug delivery by jet injectors: energetics of jet formation and penetration," *Pharm. Res.* **19**(11), 1673–1679 (2002).